Chemical stability and oxygen transport properties of La1–xCaxFe1–yByO3–δ (with B = Co, Ni, Mg) perovskite membranes

Shintaro Minami, Pierre-Marie Geffroy, Isao Kagomiya, Yuki Yamaguchi, Yasunobu Mizutani, Yusuke Ogura

Chemical stability and oxygen transport properties of $La_{1-x}Ca_xFe_{1-y}B_yO_{3-\delta}$ (with *B*=Co, Ni, Mg) perovskite membranes

Shintaro Minami[a], Pierre-Marie Geffroy[b], Isao Kagomiya[a,*], Yuki Yamaguchi[c], Yasunobu Mizutani[c] and Yusuke Ogura[d]

[a]*Department of Life Science and Applied Chemistry, Nagoya Institute of Technology, Gokiso-cho, Showa-ku, Nagoya, 466-8555, Japan*

[b]*IRCER, CNRS, Université de Limoges, CEC, 12 Rue Atlantis, 87068 Limoges, France*

[c]*Innovative Functional Materials Research Institute, Department of Materials and Chemistry, National Institute of Advanced Industrial Science and Technology (AIST), 2266-98 Anagahora, Shimo-shidami, Moriyama-ku, Nagoya, 463-8560, Japan*

[d]*Technical Research Institute, Toho Gas Co, Ltd, Tokai, 476-8501, Japan*

Keywords: oxygen semi-permeation, oxygen diffusion coefficient, oxygen incorporation, oxygen desorption, perovskite

*Corresponding author.: E-mail addresses: kagomiya@nitech.ac.jp (I. Kagomiya).

Abstract

The mixed conductive perovskite $La_{1-x}Ca_xFeO_{3-\delta}$(LCF) shows a high oxygen permeability. For the further improvement of oxygen permeability and chemical stability, this study investigates the impact of the doping elements on the perovskite B-site. The Co doping in LCF improved both of oxygen diffusion and oxygen surface exchange. However, the oxygen semi-permeation flux of Co doped LCF sample is not stable at high temperatures under the high oxygen partial pressure difference (air/argon). The Mg doping in the B site significantly improves the chemical stability of LCF membranes and the oxygen semi-permeation performances is still close to the those obtained with the Co doped LCF membranes. Thus the Mg doped LCF corresponds to best compromise between chemical stability and oxygen semi-permeation performances, which is applicable to oxygen transport membrane (OTM) or cathode in solid oxide fuel cell (SOFC).

1. Introduction

The development of electrochemical devices working at elevated temperatures with high efficient energy conversion requires the new ceramic materials with high electronic and ionic mixed conductivities, and a suitable chemical stability in working conditions. For instance, the $La_{1-x}Sr_xFe_{1-y}Co_yO_{3-\delta}$ perovskite series shows a high ionic and electronic conductivity and a high surface exchange coefficient, which correspond to good potential materials as oxygen transport membrane (OTM) or cathode in solid oxide fuel cell (SOFC) applications. Unfortunately, the chemical stability of $La_{1-x}Sr_xFe_{1-y}Co_yO_{3-\delta}$ is still not enough under low partial pressure or the chemical reactivity with oxygen separators (interconnectors) is an obstacle in SOFC devices. With the point of view, the recent works were focused on the development of ionic and electronic conductors with a good chemical stability under large range oxygen partial pressure. Then, Caro et al. [1, 2] suggest the development of Co-free perovskite membrane, as $Ba_{0.5}Sr_{0.5}Fe_{0.8}Zn_{0.2}O_{3-\delta}$ or $Ba_{0.5}Sr_{0.5}Fe_{0.9}Al_{0.1}O_{3-\delta}$, or the co-doping on the B site of the perovskite structure in view to improve the chemical stability under operating conditions. During this last decade, the works are mainly focused on the chemical stability of membrane materials during the working conditions [3, 4]. Novel cobalt free membrane materials show promising performances after long-term tests in working conditions, such as $CaTi_{0.75}Fe_{0.18}Mg_{0.09}O_{3-\delta}$ [5] or new dual-phase membranes, such as $Pr_{0.1}Gd_{0.9}Ce_{0.8}O_{2-\delta}$ / $CoFe_2O_4$ [6] or $Ce_{0.9}Pr_{0.1}O_{2-\delta}$ / $Nd_xSr_{1-x}Fe_{0.9}Cu_{0.1}O_{3-\delta}$ [7].

The $La_{1-x}Ca_xFeO_{3-\delta}$ perovskites also show a good oxygen permeability and could keep chemical stability under low oxygen partial pressure [8-11]. Our previous study investigated the systematic relation between oxygen permeability and Ca content x in $La_{1-x}Ca_xFeO_{3-\delta}$. As a result, $La_{1-x}Ca_xFeO_{3-\delta}$ in the range of x = 0.3 – 0.4 showed larger total conductivity and oxygen permeability. The activation energies of the oxygen semi-permeation flux for the x = 0.3–0.4 samples were remarkably lower among the investigated LCF samples. Particularly, J_{O2} of the x = 0.35 and 0.4 are much higher than that of the $La_{0.6}Sr_{0.4}Fe_{0.8}Co_{0.2}O_{3-\delta}$.[10] The solid oxide fuel cells (SOFCs) fabricated by using the $La_{1-x}Ca_xFeO_{3-\delta}$ (x = 0.35) as cathode showed much higher power density, compared to the case of $La_{0.6}Sr_{0.4}Fe_{0.8}Co_{0.2}O_{3-\delta}$ cathode [12]. The chemical stability of the $La_{1-x}Ca_xFeO_{3-\delta}$(LCF) perovskite in particular under CO_2 leads to study this materials for oxygen transport membrane [8, 9] and water splitting [13]. To further improvement of oxygen permeability and chemical stability based on the LCF, this study tries to investigate the impact of doping elements on the perovskite B site. With the point of view, this work investigates the chemical stability, oxygen diffusion and surface exchange coefficients of $La_{0.6}Ca_{0.4}Fe_{1-y}B_yO_{3-\delta}$ perovskite series (with B = Co, Ni, and Mg). Then, the oxygen diffusion and surface exchange coefficients (in particular oxygen incorporation and desorption coefficients) will be evaluated in this work to identify clearly the rate determining step of oxygen transport through the $La_{1-x}Ca_xFeO_{3-\delta}$ perovskite membranes.

2. Experimental procedures

2.1. Production of $La_{0.6}Ca_{0.4}Fe_{1-y}B_yO_{3-\delta}$ perovskite membranes (with B=Co, Ni, and Mg)

$La_{0.6}Ca_{0.4}Fe_{1-y}B_yO_{3-\delta}$ (with B = Co, Ni, and Mg) ceramic samples were produced by using a citrate-based liquid mixing technique.[14] La_2O_3 (99.99% purity) was at first pre-heated at 1000 °C for 8 h in ambient air to remove the moisture or CO_2 included in the powders. The La_2O_3 and $CaCO_3$ (99.9% purity) were weighed and dissolved in nitric acid. In the case of Mg doped sample, MgO (99.9 % purity) was also dissolved in nitric acid. $Fe(NO_3)_3{\cdot}9H_2O$ (99.9% purity) was weighed and dissolved in deionized water. For the Co or Ni doped sample, $Co(NO_3)_3{\cdot}9H_2O$ (99.9% purity) or $Ni(NO_3)_2{\cdot}6H_2O$ (99.9 % purity) was also weighed and dissolved in deionized water. To the mixture of the solutions, citric acid (≥ 99.5% purity) and ethylene glycol (≥ 99.5% purity) were added, and the solution afforded a gel during heating it at 300 °C for 2 h. The obtained gel was heat-treated at 450 °C for 1 h and was then degreased at 600 °C for 10 h. The precursor powders for y = 0 and y = 0.1, 0.2 was calcined at 900 °C and 950 °C, respectively for 10 h. The calcined powders were molded into a pellet by using a die with the diameter of 32 mmϕ and then pressed under 300 MPa pressure by using a cold isostatic pressing machine (CIP). For the B-site non doped sample and Co and Ni doped sample, pressed pellets were sintered at 1300 °C for 10 h in ambient air. The pressed sample doped with Mg was sintered at 1250 °C for 10 h in ambient air.

2.2. Characterizations

The crystalline phases of the prepared samples at room temperature were investigated using an usual x-ray powder diffractometer (XRPD; RAD-C; Rigaku Corp.) with Cu Kα radiation (incident wavelength λ_i= 1.5418 Å) at ambient temperature. The respective conditions of XRPD voltage and current were 45 kV and 40 mA. To remove the Cu $K\beta$ as well as the other radiation deriving from the x-ray fluorescence, a Ge monochromator was used.

2.3. Oxygen semi-permeation measurements

The oxygen semi-permeation measurements were performed using a homemade device described in a previous work [15]. It is built with a central reactor where the dense membrane is inserted between two chambers with two different oxygen partial pressures. In each chamber, two microelectrodes (gold and zirconia tip electrodes) in contact with the membrane surface allow determining the oxygen potential gradients between the membrane surface and the gas at the vicinity of the membrane surface.

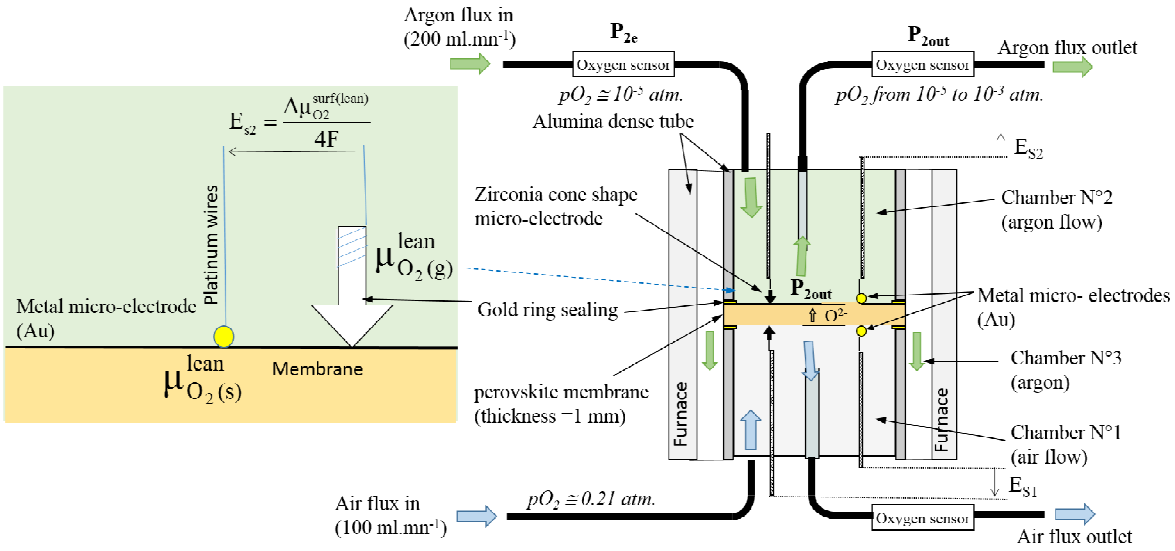

Figure 1: Setup for oxygen semi-permeation measurements with the zirconia cone shape and gold microelectrodes for the measures of oxygen activity at the membrane surfaces [15].

Gas flow was imposed upon each of the opposite faces (synthetic air to the lower surface and argon to the upper surface), producing an oxygen partial pressure gradient. In the temperature range of 600-1000 °C, the oxygen content in the argon was monitored using a YSZ-oxygen sensor.

The oxygen sensor provides an electromotive force (noted E) in accordance with the Nernst law. Oxygen semi-permeation fluxes can be calculated from the value of P_{2out} and Eq. 1 when the oxygen flow ($J_{O_2} \times S$) through the membrane (here in $ml.s^{-1}$) is significantly lower than the inlet argon flow in chamber 2, corresponding to 200 $ml.s^{-1}$. In general, an argon atmosphere is preferred for the oxygen flux measurements, to achieve higher sensitivity and accuracy for low variations in the oxygen content.

The oxygen flux through the membrane is evaluated using the following equation:

$$J_{O_2} = \frac{D_{Ar}}{S\ V_{m(Ar)}}\ (P_{2out} - P_{2e}) \quad \textbf{(Eq. 1)}$$

where $J_{O_2}$is the oxygen flux through the membrane in mol.m^{-2}.s^{-1}, D_{Ar} the argon flow in l.s^{-1}, $V_{m(Ar)}$ the molar volume of argon in l.mol^{-1} and S the effective membrane surface in m². P_{2out} and P_{2e} are the oxygen partial pressure in the outlet argon flux and the oxygen partial pressure in the argon flux (in atm), respectively.

The oxygen partial pressures in gas flows are evaluated from the electromotive force $E_{(g)2out}$, measured by YSZ-oxygen sensors, following the Nernst law:

$$E_{(g)2out} = \frac{RT}{4F} ln \frac{P_{2out}}{P_{O_2}} \quad \textbf{(Eq. 2)}$$

where R is the universal gas constant, F is the Faraday constant, T is the temperature and P_{O2} is the oxygen partial pressure in the air (= 0.21 atm.).

The particularity of this apparatus is the possibility to determine the oxygen activity at the both surfaces of the membrane. The microelectrodes system, composed of a gold electrode and a zirconia tip, in contact with the surface measures two electromotive forces E_{s1} and E_{s2}, corresponding to the variation of oxygen activities between the inlet gas and the oxygen-rich or lean surfaces of the membrane [15]. The gradients of di-oxygen activity on each surface of the membrane are evaluated from the Nernst law:

$$E_{S1} = \frac{RT}{4F} ln \frac{a_1}{a\prime_1} = \frac{\Delta\mu_{O_{2(s)}}^{rich}}{4F} \quad \textbf{(Eq. 3)}$$

$$E_{S2} = \frac{RT}{4F} ln \frac{a\prime_2}{a_2} = \frac{\Delta\mu_{O_{2(s)}}^{lean}}{4F} \quad \textbf{(Eq. 4)}$$

where $\Delta\mu_{O_{2(s)}}^{lean} = \mu_{O_{2(s)}}^{lean} - \mu_{O_{2(g)}}^{lean}$ and $\Delta\mu_{O_{2(s)}}^{rich} = \mu_{O_{2(g)}}^{rich} - \mu_{O_{2(s)}}^{rich}$

$\mu_{O_{2(g)}}^{rich}$ and $\mu_{O_{2(g)}}^{lean}$ are the oxygen chemical potentials in air and argon. $\mu_{O_{2(s)}}^{rich}$ and $\mu_{O_{2(s)}}^{lean}$ are the oxygen chemical potentials on oxygen-rich and oxygen-lean surfaces, respectively. The difference between the oxygen chemical potential $\mu_{O_{2(s)}}^{lean}$ and $\mu_{O_{2(s)}}^{rich}$ corresponds to the gradient of oxygen chemical activity in the bulk of the membrane, noted $\Delta\mu_{O_2}^{Bulk}$. Then, the coefficient of oxygen diffusion (D_O), expressed in $cm^{-2}.s^{-1}$, is calculated with the following equation:

$$D_0 = \frac{4LJ_{O_2}}{C_0\Delta\mu_{O_2}^{Bulk}} \quad \textbf{(Eq. 5)}$$

k_i and k_{des} are respectively the kinetic coefficients of oxygen surface exchange at oxygen-rich surface and at oxygen-lean surface of the membrane, expressed in $cm.s^{-1}$. They are described from the formalism recently reported by Bazan et al. [16] or Adler et al. [17] and calculated from the oxygen semi-permeation flux and the gradient of oxygen chemical potential at the membrane surface, as following:

$$k_i = 2J_{O_2} \Big/ \left(C_0^{rich} \left(exp\left(\frac{(1-n)\Delta\mu_{O_{2(s)}}^{rich}}{2RT} \right) - exp\left(\frac{-n\Delta\mu_{O_{2(s)}}^{rich}}{2RT} \right) \right) \right) \quad \textbf{(Eq. 6)}$$

$$k_{des} = 2J_{O_2} \Big/ \left(C_0^{lean} \left(exp\left(\frac{(1-n)\Delta\mu_{O_{2(s)}}^{lean}}{RT} \right) - exp\left(\frac{-n\Delta\mu_{O_{2(s)}}^{lean}}{RT} \right) \right) \right) \quad \textbf{(Eq. 7)}$$

where n is a coefficient typically equal to 0.5 for MIEC materials and C_0^{rich} and C_0^{lean} are the oxygen molar concentrations at the oxygen-rich and oxygen-lean surface, respectively. C_0 is estimated by $C_o = (3-\delta)/V_m$, where V_m is the molar volume estimated by XRD patterns and δ

is the oxygen under-stoichiometry. The δ is assumed at 0.2-0.3 at 900°C on the basis of the oxygen nonstoichiometry investigated in analogous perovskites $Ln_{0.5}A_{0.5}FeO_{3-\delta}$ (Ln = La - Sm, *A*=Ba, Sr) [18].

3. Results and discussion

3.1. XRPD patterns of the prepared $La_{1-x}Ca_xFe_{1-y}B_yO_{3-\delta}$ (LCFB; B = Co, Ni, Mg)

Figure 2 shows XRPD patterns of the prepared $La_{0.65}Ca_{0.35}FeO_{3-\delta}$(LCF6535), $La_{0.6}Ca_{0.4}FeO_{3-\delta}$ (LCF64), $La_{0.6}Ca_{0.4}Fe_{0.8}Co_{0.2}O_{3-\delta}$(LCFCo6482), $La_{0.6}Ca_{0.4}Fe_{0.9}Ni_{0.1}O_{3-\delta}$(LCFNi6491) and $La_{0.6}Ca_{0.4}Fe_{0.9}Mg_{0.1}O_{3-\delta}$ (LCFMg6491) samples. The XRPD patterns in each sample corresponds to orthorhombic perovskite with space group of *Pnma*. No secondary phases appeared in LCF6535, LCF64, LCFCo6482, LCFNi6491, whereas the reflection corresponding to a secondary phase appeared in LCFMg6491. The reflection observed around $2\theta = 37°$ in LCFMg6491 comes from MgO. Table 1 lists lattice volumes evaluated from the XRPD patterns. The lattice volumes of LCFCo6482, LCFNi6491were smaller than that of LCF64. Table 2 lists the ionic radius of Fe, Co, Ni and Mg ions [19]. The comparison of ionic radius suggests that the main substituted ions in LCFCo6428 and LCFNi6491 are Co^{3+} and Ni^{3+}, respectively. The lattice volume of LCFMg6491 was larger than that of LCF64, suggesting that larger Mg^{2+} ions are

partially substituted for the Fe^{3+} ions although the MgO secondary phase appears in LCFMg6491.

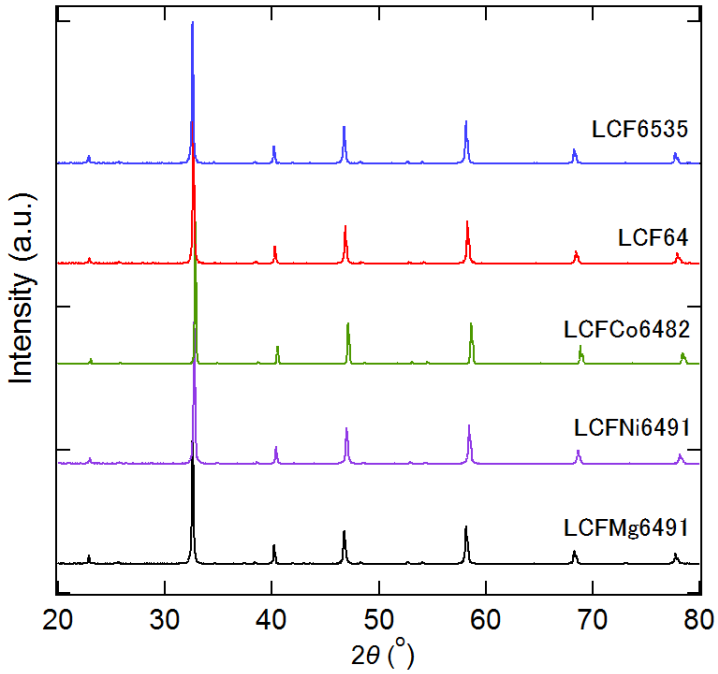

Figure 2: XRPD patterns of the prepared $La_{0.65}Ca_{0.35}FeO_{3-\delta}$ (LCF6535), $La_{0.6}Ca_{0.4}FeO_{3-\delta}$ (LCF64), $La_{0.6}Ca_{0.4}Fe_{0.8}Co_{0.2}O_{3-\delta}$ (LCFCo6482), $La_{0.6}Ca_{0.4}Fe_{0.9}Ni_{0.1}O_{3-\delta}$ (LCFNi6491) and $La_{0.6}Ca_{0.4}Fe_{0.9}Mg_{0.1}O_{3-\delta}$ (LCFMg6491).

Table 1 Lattice volume of the prepared LCF*B* (*B* = Co, Ni, Mg) samples.

Sample	Lattice volume (Å^3)
LCF6535	233.1(2)
LCF64	231.2(2)
LCFCo6482	228.1(2)
LCFNi6491	229.5(2)
LCFMg6491	232.8(2)

Table 2 Effective ionic radii of each ion under the condition of coordination number of 6 [19].

Ion	Ionic radii (Å)
Fe^{3+} (high spin)	0.645
Fe^{4+}	0.585
Mg^{2+}	0.720
Co^{3+} (high spin)	0.61
Co^{4+} (high spin)	0.53
Ni^{2+}	0.690
Ni^{3+} (high spin)	0.60

3.2. Oxygen semi-permeation flux through LCFB perovskite membranes (with B = Co, Ni, and Mg).

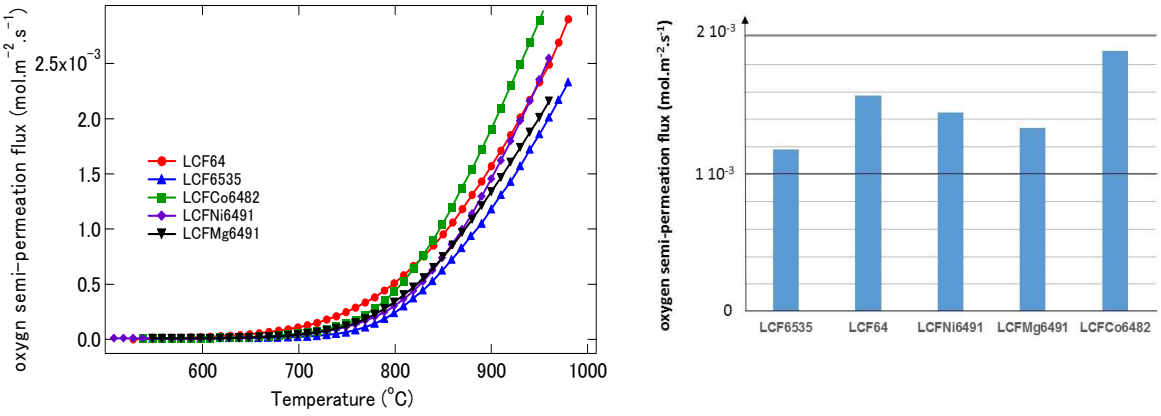

a) b)

Figure 3: Oxygen flux through LCF*B* perovskite membranes a) during the cooling and b) comparative oxygen flux of $La_{1-x}Ca_xFeO_{3-\delta}$ perovskite membranes at 900°C.

Figure 3 shows the comparative study of oxygen semi-permeation flux through LCF6535,

LCF64, LCFCo6482, LCFNi6491, LCFMg6491 membranes. LCFCo6482 membrane has the largest oxygen fluxes, and LCF6535 membrane has the lowest oxygen fluxes at 900°C among the investigated samples, as presented on Fig. 3b). Besides, it notes that the LCF6535 membrane has lower oxygen semi-permeation fluxes than one obtained with LCF64 membrane, in opposition with previous work [10]. However, the oxygen semi-permeation fluxes obtained with LCF6535 and LCF64 membranes in these works are still very close and in agreement with values obtained in previous work, 1.2 and 1.8 x 10^{-3} mol.m^{-2}.s^{-1} at 900°C, respectively.

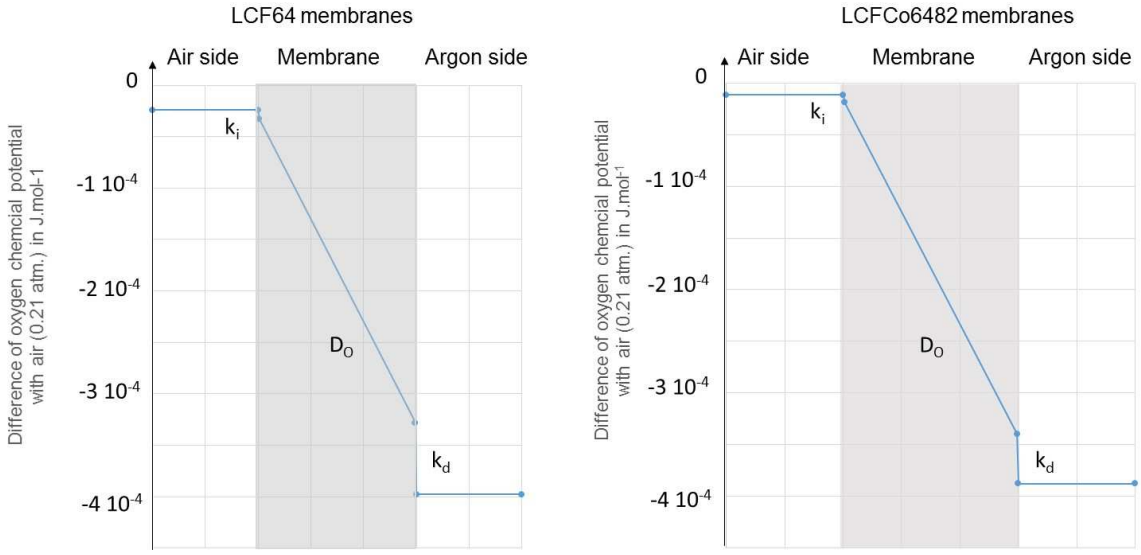

Figure 4: Oxygen chemical potential profile through a) LCF64 and b) LCFCo6482 membranes.

The micro-electrode systems of the set up allows to determine the oxygen activities at the both sides of the membrane and the profile of oxygen potential through the membrane. Figure 4 shows the oxygen chemical potential profiles at 900°C through LCF64 and LCFCo6482 membrane

respectively. The relative gradients of oxygen chemical potential at the both side of the surface are very low in comparison with the gradients of oxygen chemical potential through the bulk of the membrane. Indeed, it notes similar oxygen chemical profiles through $La_{0.6}Ca_{0.4}Fe_{1-y}B_yO_{3-\delta}$ perovskite membranes (with B = Co, Ni, and Mg). This shows that the oxygen semi-permeation flux through $La_{0.6}Ca_{0.4}Fe_{1-y}B_yO_{3-\delta}$ perovskite membranes (with B = Co, Ni, and Mg) is governed mainly by the oxygen diffusion in the bulk at 900°C, and not by the surface exchange kinetics (with thickness =1.5 mm).

Table 3: oxygen diffusion, incorporation and desorption surface exchange coefficients of $La_{0.6}Ca_{0.4}Fe_{1-y}B_yO_{3-\delta}$ perovskites (with B = Co, Ni, and Mg) at 800°C and 900°C under gradient air/argon.

Materials	D_O ($cm^2.s^{-1}$)		k_i ($cm.s^{-1}$)		k_d ($cm.s^{-1}$)	
	800°C	900°C	800°C	900°C	800°C	900°C
$La_{0.8}Ca_{0.2}FeO_{3-\delta}$ [20]	(D_O) 5 10^{-8}	-	(k) 10^{-6}	-	(k) 10^{-6}	-
LCF6535	4.4 10^{-8}	2.9 10^{-7}	1.1 10^{-5}	5 10^{-5}	1 10^{-5}	4.5 10^{-5}
LCF64	**1.1 10^{-7}**	4 10^{-7}	2.2 10^{-5}	1 10^{-4}	2 10^{-5}	7 10^{-5}
LCFMg6491	7 10^{-8}	3.4 10^{-7}	1.2 10^{-4}	1.3 10^{-4}	**3.6 10^{-5}**	4.5 10^{-5}
LCFCo6482	8 10^{-8}	**4.7 10^{-7}**	**3.6 10^{-5}**	**1.4 10^{-4}**	**3.6 10^{-5}**	**1.3 10^{-4}**
LCFNi6491	6 10^{-8}	3.5 10^{-7}	1.2 10^{-5}	7 10^{-5}	1.2 10^{-5}	6 10^{-5}

From the determination of oxygen activities at both surfaces of the membrane, it is possible to evaluate the average oxygen diffusion, oxygen incorporation and desorption coefficients of the membrane materials in relation with the temperature, as reported in section 2.3. These coefficients are reported in Table 3 for $La_{0.6}Ca_{0.4}Fe_{1-y}B_yO_{3-\delta}$ perovskite materials (with B = Co, Ni, and Mg). The LCFCo6482 perovskite has the higher coefficient of diffusion (4.7 10^{-7} $cm^2.s^{-1}$ at 900°C) and surface exchange (incorporation 1.4 10^{-4} $cm.s^{-1}$, and desorption 3.6 10^{-5} $cm.s^{-1}$ at 900°C). However at 800°C, LCF64 perovskite shows a similar value of coefficients and oxygen semi-permeation performances of LCFCo6482 perovskite. Then at lower temperatures (below 800°C), it notes on the Fig. 3 that LCF64 membrane has the highest oxygen permeation flux in the investigated samples.

Besides, it notes that the coefficients of incorporation is always higher or equal to the coefficients of desorption. In other works, the kinetics coefficient of oxygen incorporation at the surface in contact with air are higher than those of oxygen desorption at the surface in contact with argon, as reported in previous works [20]. The oxygen diffusion and surface exchange coefficients of $La_{0.8}Ca_{0.2}FeO_{3-\delta}$ have been evaluated at D_o~5 10^{-8} $cm^2.s^{-1}$ and k~10^{-6} $cm^2.s^{-1}$ at 800 °C under 10^{-2} bar P_{O2} by electrical conductivity relaxation method [21]. Thus the oxygen diffusion and surface exchange coefficients of LCF64 is very similar to those of the analogous LCF. The oxygen diffusion and surface exchange coefficients of similar perovskite materials, such as

$CaTi_{0.9}Fe_{0.1}O_{3-\delta}$ perovskite, have been recently evaluated at 5.5 10^{-8} $cm^2.s^{-1}$ and 8 10^{-7} $cm.s^{-1}$ at 900°C under air by isotopic exchange method [22].

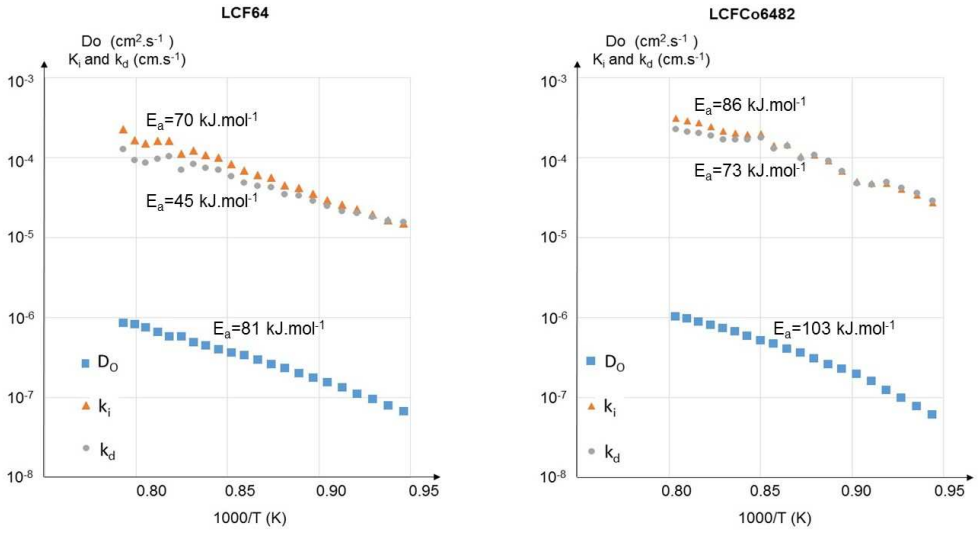

Figure 5: Arrhenius plot of k_i, k_d and D_O coefficients of LCF64 and LCFCo6482 perovskite.

Figure 5 shows the Arrhenius plots of k_i, k_d and D_O coefficients of LCF64 and LCFCo6482 perovskite. The energy activation of oxygen flux through the membranes is similar to the energy activation of D_O, since the oxygen flux is governed mainly by the oxygen diffusion in the bulk of the membrane. Then, these values are a good agreement with the data reported by S. Diethelm et al. [8] for the similar materials, for LCF64 E_a=107 kJ.mol^{-1} (81 kJ.mol^{-1} in this work), and for LCFCo6482 E_a=115 kJ.mol^{-1} (103 kJ.mol^{-1} in this work). It notes that the activation energy increases slightly with Co doping in B site of perovskite structure, whereas the oxygen diffusion coefficient increases with Co doping in B site (at high temperature > 700°C).

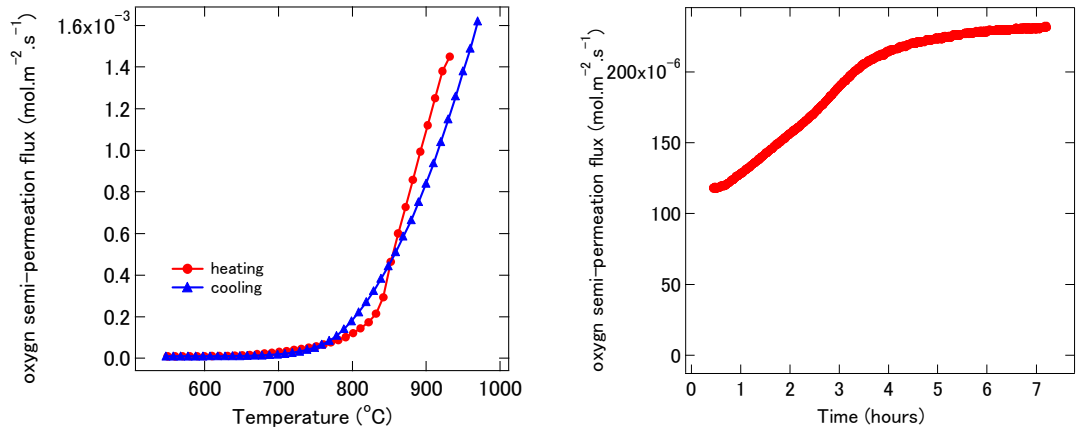

a) b)

Figure 6: Oxygen flux through LCF6535 a) during the heating and the cooling from 500°C to 970°C, b) Evolution of oxygen flux for LCF6535 sample in isothermal conditions at 810°C after heating from 500°C to 810°C (5°C.min^{-1})

Figure 6 a) shows the oxygen flux through LCF6535 during heating and cooling. The oxygen flux during heating and cooling at the lower temperature than 750°C are almost same. However, the oxygen flux during cooling at the temperature from 750 to 850°C is larger than during heating. It notes a large and anomalous increase of oxygen flux during the heating between 820 and 850°C. Indeed, we assume that the oxygen flux during heating is impacted by the phase transform from the orthorhombic to rhombohedral close 820-850°C. The recent study shows that the crystalline phase of the LCF6535 transforms is between 600 and 800°C [10], so it is assumed that the transform of the LCF6535 during heating occurred very slowly. Figure 6 b) shows the evolution

of the oxygen flux for LCF6535 sample in isothermal conditions at 810°C (after a long period at 500°C). The oxygen flux increased at 810°C and then is constant after about 7 hours. Therefore, this evolution of flux is possibly linked to the phase transformation from orthorhombic to rhombohedral of the LCF6535 perovskite during heating is very slowly.

3.3. Comparative study of chemical stability of $La_{0.6}Ca_{0.4}Fe_{1-y}B_yO_{3-\delta}$ perovskite membranes (with B=Co, Ni, and Mg)

Figure 7 shows the evolution of relative flux during heating for 24 h at 900°C and 950°C for LCF6535, LCFNi6491, LCFCo6482 and LCFMg6491 membranes under air/argon gradients. It notes that the Mg doping leads to improve the stability of oxygen flux at 900°C and 950°C. Then, the oxygen flux is very stable at 900°C for LCFMg6491 membranes, with relative variation of oxygen flux after 24h of -0.4%. In opposite, the oxygen flux of LCFNi6491, LCFCo6482 membranes at 900°C and 950°C decreases significantly linked likely to insufficient chemical stability of perovskite phase.

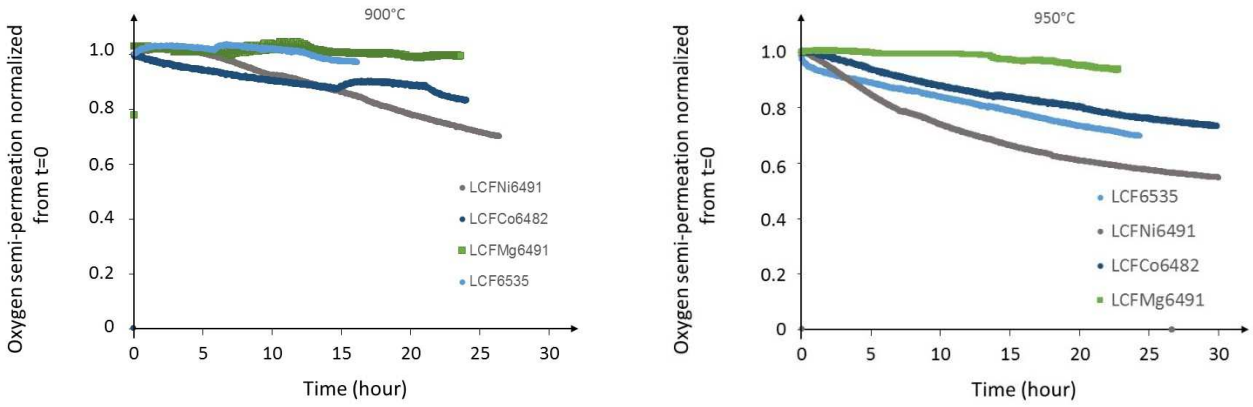

a) b)

Figure 7: Evolution of relative flux at a) 900 and b) 950°C after 24h. The flux is normalized in comparison with the initial flux of membranes at $t = 0$ hour.

Table 4 shows chemical stability under working conditions (air/argon gradient). The chemical stability of LCFMg6491 is the highest in the other investigated compositions, but the chemical stability of LCFCo6482 is the lowest at 900°C of the other compositions, as expected.

Table 4 Chemical stability under working conditions (air/argon gradient)

Materials	Flux relative variation of flux /cycle	Variation after 24h 900°C	Variation after 24h 950°C
LCF6535	-14%	-3.3%	-30%
LCFNi6491	-13%	-26%	-40%
LCFMg6491	-8%	-0.4%	-6%
LCFCo6482	-24%	-16%	-24%

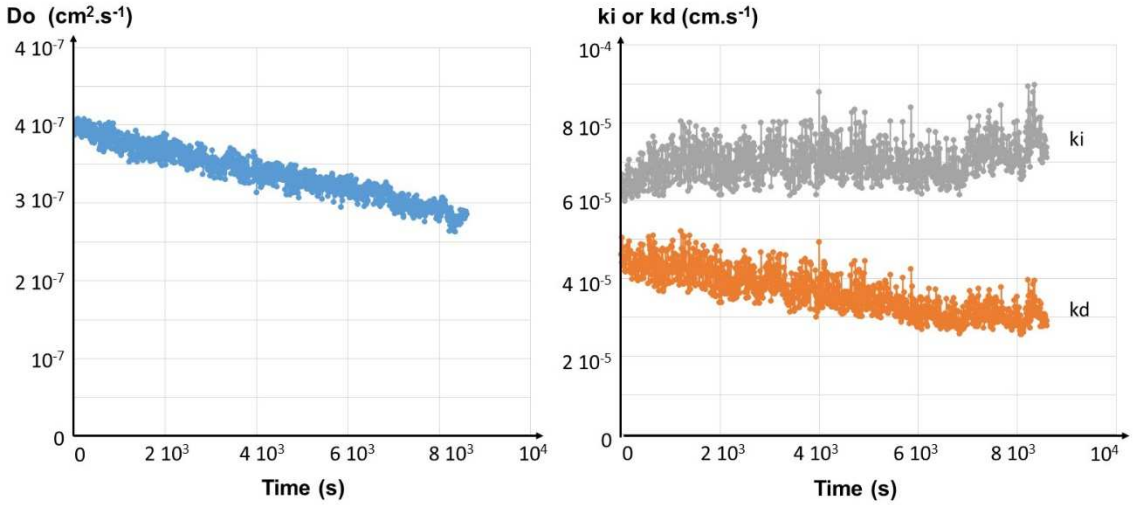

Figure 8: Evolution of average D_o in thickness of membranes and the k_i and k_d coefficients at 950°C for LCF6535 membranes.

Figure 8 shows the evolution during 24 hours of D_O, k_i and k_d at 950°C for LCF6535 membranes at 950°C, under a gradient air/argon. The D_O and k_d coefficients decrease significantly, while the k_i is stable. Then, it assumes that the decreasing of oxygen semi-permeation performances is linked to the physico-chemical evolution of LCF6535 perovskite phase at the surface in contact with low oxygen partial pressure atmosphere. We assume here that there is not the chemical

decomposition of materials in the membrane bulk (as confirmed by XRD patterns before and after oxygen semi-permeation measurements in additional information, Fig. S1. The physico-chemical evolution at the material surface can be associated to likely low kinetics of the ordering of the surface, as reported for the similar perovskite materials [23]. This physico-chemical evolution leads also to decrease of k_d and the apparent oxygen diffusion coefficients at the vicinity the membrane surface. Then, the partial degradation of membrane performances at the permeate side has observed for the similar materials by S. Diethelm et al. [8].

4. Conclusion

This study prepared LCF*B* (*B* = Co, Ni, Mg) ceramic samples. The B-site doping improved oxygen surface exchange $k_{ex.}$ The oxygen diffusion coefficient D_O of LCFCo6428 was the largest in the prepare sample. Thus the Co doping in LCF is beneficial to improve both of oxygen diffusion and oxygen surface exchange. However, the oxygen semi-permeation flux of Co doped LCF sample is not stable at high temperatures under air/argon (about 10^{-4} atm.).

The Mg doping in B site improves significantly the chemical stability of LCF membranes and the oxygen semi-permeation performances of LCFMg6491 membranes is still close to the performances obtained with the LCFNi6491 and LCFCo6482 perovskite membranes. Thus LCFMg6491 perovskite membranes correspond to the best compromise between chemical

stability and oxygen semi-permeation performances, in particular when the operating working is lower than 800°C.

References

[1] K. Efimov, T. Halfer, A. Kuhn, P. Heitjans, J. Caro, A. Feldhoff, Chem. Mater. 22 (2010) 1540.

[2] X. Chen, H. Liu, Y. Wie, J. Caro, H.H. Wang, J. Alloys and Compounds 484 (2009) 386.

[3] Y. Zou, F. Schulze-Küppers, J. Malzbender, Creep behavior of porous $La_{0.6}Sr_{0.4}Co_{0.2}Fe_{0.8}O_{3-\delta}$ oxygen transport membrane supports. Ceram. Inter., 41 (3) (2015) 4064-4069.

[4] B.X. Huang, R. W. Steinbrech, S. Baumann, S., Creep behavior and its correlation with defect chemistry of $La_{0.58}Sr_{0.4}Co_{0.2}Fe_{0.8}O_{3-\delta}$. Acta Materialia, 66 (6) (2012) 2479-2484.

[5] M. Balanguer, S. Escolastico, J.M. Serra, Oxygen permeation and stability of $CaTi_{0.75}Fe_{0.18}Mg_{0.09}O_{3-\delta}$ oxygen-transport membrane, J. Membr. Sci. 524 (2017) 56-63.

[6] X. Bi, X. Meng, P. Liu, N. Yang, Z. Zhu , R. Ran, S. Liu, A novel CO2-resistant ceramic dual-phase hollow fiber membrane for oxygen separation, J. Membr. Sci. 522 (2017) 91-99.

[7] G. Chen, Z. Zhao, M. Widenmeyer, R. Yan, L. Wang, A. Feldhoff, A. Weidenkaff, Synthesis and Characterization of 40 wt % $Ce_{0.9}Pr_{0.1}O_{2-\delta}$–60 wt % $Nd_xSr_{1-x}Fe_{0.9}Cu_{0.1}O_{3-\delta}$ Dual-Phase Membranes for Efficient Oxygen Separation, Membranes 10 (2020) 183.

[8] S. Diethelm, J. Van herle, P.H. Middleton, D. Favrat, Oxygen permeation and stability of $La_{0.4}Ca_{0.6}Fe_{1-x}Co_xO_{3-\delta}$ (x = 0, 0.25, 0.5) membranes, Journal of Power Sources, 118 (2) (2003) 270-27.

[9] D. Yang, N. Yang, B. Meng, X. Tan, C. Zhang, J. Sunars, Z. Zhu, S. Liu, A-site excess

$(La_{0.8}Ca_{0.2})_{1.01}FeO_{3-\delta}$ (LCF) perovskite hollow fiber membrane for oxygen permeation in CO_2-containing atmosphere, Energy Fuels 31 (2017) 4531–4538.

[10] I. Kagomiya, T. Murayama, K. Tsunekawa, K.-I. Kakimoto, Y. Ogura, Crystalline phase and oxygen permeation properties of mixed conductive, J. Euro. Cerm. Soc. 29 (2019) 1082-1092.

[11] I. Kagomiya, T. Takahashi, K. Kakimoto, Oxide ion conduction and surface exchange reactions of mixed conductive $La_{0.65}Ca_{0.35}FeO_{3-\delta}$ based on oxygen permeation Study, Chem. Mater., 31 (2019) 10135-10142.

[12] Y. Yamaguchi, I. Kagomiya, S. Minami, H. Shimada, H. Sumi, Y. Ogura, Y. Mizutani, $La_{0.65}Ca_{0.35}FeO_{3-\delta}$ as a novel Sr- and Co-free cathode material for solid oxide fuel cells, J. Power Sources, 448 (2020) 227426.

[13] Xing Zhu, Congzhi Shi, Kongzhai Li, Kang Zhai, Hua Wang, Yonggang Wei, Dong Tian, Chunhua Zeng, Water splitting for hydrogen generation over lanthanum-calcium-iron perovskite-type membrane driven by reducing atmosphere, Int. J. Hydrogen Energy, 42 (31) (2017) 19776-19787.

[14] M.P. Pechini, U.S. Patent #3330697, 1967.

[15] P.-M. Geffroy, A. Vivet, J. Fouletier, C. Steil, E. Blond, N. Richet, P. Del Gallo, T. Chartier, The impact of experimental factors on oxygen semi-permeation measurements, J. Electrochem. Soc., 160 (1) (2013) F1-F9.

[16] M.Z. Bazant, Theory of chemical kinetics and charge transfer based on nonequilibrium thermodynamics, Accounts of chemical research, 46, 5 (2013) 1144-1160.

[17] S.B. Adler, X.Y. Chen, J.R. Wilson, Mechanisms and rate laws for oxygen exchange on mixed-conducting oxide surfaces, Journal of Catalysis, 245 (2007) 91-109.

[18] V.V. Kharton, A.V. Kovalevsky, M.V. Patrakeev, E.V. Tsipis, A.P. Viskup, V. A. Kolotygin, A.A. Yaremchenko, A.L. Shaula, E.A. Kiselev, J.C. Waerenborgh, Oxygen nonstoichiometry, mixed conductivity, and Mössbauer Spectra of $Ln_{0.5}A_{0.5}FeO_{3-\delta}$ (Ln = La-Sm, A = Sr, Ba) : Effects of Cation Size, Chem. Mater., 20 (2008) 6457-6467.

[19] R.D. Shanon, Revised effective ionic radii and systematic studies of interatomic distances in halides and chalcogenides, Acta Cryst., A32 (1976) 751-767.

[20] P.-M. Geffroy, E. Blond, N. Richet, T. Chartier, Understanding and identifying the oxygen transport mechanisms through mixed-conductor membranes, Chem. Eng. Sci., 162 (2017) 245-261.

[21] C. Berger, E. Bucher, A. Windischbacher, A. Daniel Boese, W. Sitte, Strontium-free rare earth perovskite ferrites with fast oxygen kinetics: experiment and theory, J. Sol. Stat. Chem., 259 (2018) 57-66.

[22] C. Salles, J.M. Bassat, J. Fouletier, D. Marinha, M.-C. Steil, Oxygen pressure dependence of the ionic conductivity of iron-doped calcium titanate, *Solid State Ionics*, 324 (2018) 103–108.

[23] D. Kim, J. Wan Park, B.-H. Yun, J. Hwa Park, K.T. Lee, Correlation of Time-Dependent Oxygen Surface Exchange Kinetics with Surface Chemistry of $La_{0.6}Sr_{0.4}Co_{0.2}Fe_{0.8}O_{3-\delta}$ Catalysts, *ACS Appl. Mater. Interfaces,* 11, 35 (2019) 31786–31792.

Additional information

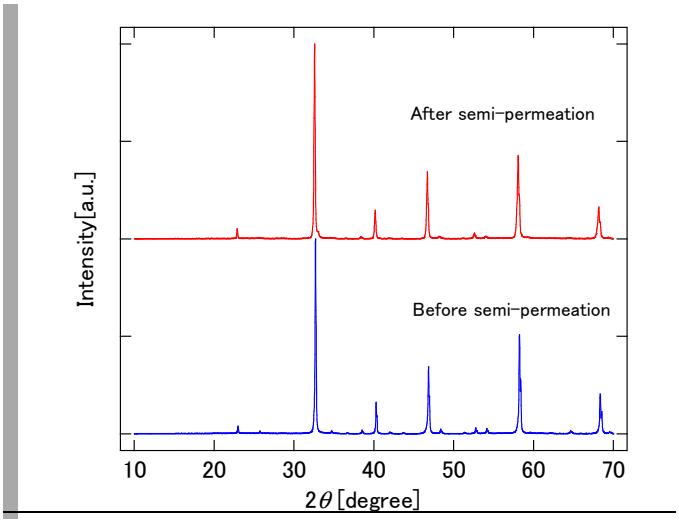

Figure S1: XRD for LCF6535sample-after and before semi-permeation measurement during 24 hours.